Polymer Chemistry

ROYAL SOCIETY OF CHEMISTRY

PAPER

View Article Online
View Journal | View Issue

Cite this: *Polym. Chem.*, 2024, **15**, 553

Enhanced thermal and porous properties of double-decker-shaped polyhedral silsesquioxane-bismaleimide (DDSQ-BMI) nanocomposites for high-performance CO_2 storage and supercapacitors†

Zih-Yu Chen, Wei-Cheng Chen and Shiao-Wei Kuo *

Received 6th October 2023,
Accepted 2nd January 2024

DOI: 10.1039/d3py01115a

rsc.li/polymers

In this study, we employed nadic anhydride (ND), which was covalently bound to double-decker silsesquioxane (**DDSQ**) by hydrosilylation. The terminal aromatic diamine was connected to **DDSQ-ND** by maleic anhydride (MA) through a dehydration reaction to form DDSQ-bismaleimide (DDSQ-BMI) products. The values of thermal decomposition temperature (T_d) and char yield were significantly increased after thermal curing of DDSQ-BMI products as compared to pure BMI without the **DDSQ** inorganic cage. Among the various thermal curing procedures, **DDSQ-MDA-BMI** heated at 480 °C for 6 h possessed a highly microporous structure with a significantly large surface area (826 m^2 g^{-1}) and displayed high CO_2 gas storage and capture at 273 K under 1.0 bar (7.71 wt%). In addition, it displayed excellent specific capacitance (73.66 F g^{-1}) and satisfactory capacitance retention (86.4%).

Introduction

Porous organic polymers (POPs) integrate porous structures and subsequently acquire unique properties that can be utilized in various applications such as gas (CO_2 or H_2) storage, catalysis, removal of pollutants from air or water *via* adsorption, sensing, and drug delivery.[1–10] The advantage of POPs is that by mediating the chemical structures of monomers or synthetic methodologies, POPs can be produced with variable pore size and volume, chemical functionality or surface area.[11–15] The various POPs are produced by synthetic approaches that incorporate conjugated microporous polymers (CMP), covalent organic frameworks (COF), covalent triazine frameworks, and hyper-crosslinked polymers (HCP), and they are constructed using imine, azine, imide and triazine linkages.[16–20]

The conventional approach for synthesizing HCPs involves Friedel–Crafts alkylation, albeit with the associated drawbacks of environmentally unfriendly generation of harmful byproducts and use of volatile solvents.[21,22] As a result, an alternative approach for HCP synthesis based on free radical polymerization using bismaleimide (BMI) derivatives has been investigated with green and atom-economical procedures.[23–25] Bismaleimide can effectively decrease the generation of harmful chemicals due to its additive reactions. With its accessibility and low cost, it has recently displayed outstanding performance in the industry.[26,27] It is currently widely employed in the fields of circuit boards, electronics, defense and aerospace.

BMI monomers can form a three-dimensional network through thermal cross-linking at high temperatures without any initiator, which enables them to perform admirably in terms of high-temperature resistance and high-strength. However, unmodified BMI have some disadvantages, including high melting point, high curing temperature and brittleness. Extensive research has been performed to increase the hardness of BMI through copolymerization or homopolymerization with substances, such as cyanate esters, epoxy resins and aromatic amines, and a compromise is made between the required mechanical properties and thermal resistance of the modified BMI.[28,29]

There are also some challenges related to the stability of POPs, which may limit their long-term use in certain applications, and thus, there have been numerous efforts to increase their stability and optimize their properties.[30–33] In pursuit of improved thermal properties for BMI derivatives, in our previous study, we proposed the incorporation of inorganic nanoparticles such as double-decker-shaped

Department of Materials and Optoelectronic Science, Center for Functional Polymers and Supramolecular Materials, National Sun Yat-Sen University, Kaohsiung 80424, Taiwan. E-mail: kuosw@faculty.nsysu.edu.tw

† Electronic supplementary information (ESI) available. See DOI: https://doi.org/10.1039/d3py01115a

polyhedral silsesquioxane (**DDSQ**).[34] In polymer/**DDSQ** or polymer/POSS hybrids,[35–46] there is high thermal stability because of their intrinsic inorganic cage structure, which can increase the thermal decomposition temperatures of BMI resins using physical dispersion or chemical covalent bonding.

In this study, two distinct types of BMI-based **DDSQ** monomers were synthesized through nadic anhydride (ND) and were covalently linked with double-decker silsesquioxane (**DDSQ**) by hydrosilylation. Both ends of the aromatic diamine were coupled with **DDSQ-ND** using maleic anhydride (MA) in separate reactions, resulting in the creation of **DDSQ**-bismaleimides named **DDSQ-MDA-BMI** and **DDSQ-MPD-BMI**.

Following meticulous control over the thermal curing procedures, thermal treatment of **DDSQ-MDA-BMI** at 480 °C for 6 h resulted in a microporous structure formation with a significantly large surface area (826 m^2 g^{-1}), satisfactory CO_2 gas storage and capture performance at 273 K under 1.0 bar (7.71 wt%). **DDSQ-MDA-BMI** also displayed excellent specific capacitance (73.66 F g^{-1}) and maintained satisfactory capacitance retention (86.4%).

Experimental section

Materials

4,4-Diaminodiphenylmethane (MDA), *m*-phenylenediamine (MPD), maleic anhydride (MA), acetic anhydride, *N*,*N*-diethylethanamine, toluene and acetone were purchased from Sigma-Aldrich. **DDSQ-ND** was synthesized according to a previously published procedure.[34,35,42,43]

Synthesis of DDSQ-ND-MDA and DDSQ-ND-MPD

DDSQ-ND (5.9 g, 4 mmol) and excess MDA (4.8 g, 24 mmol) or MPD (2.6 g, 24 mmol) were placed into a flask with a reflux

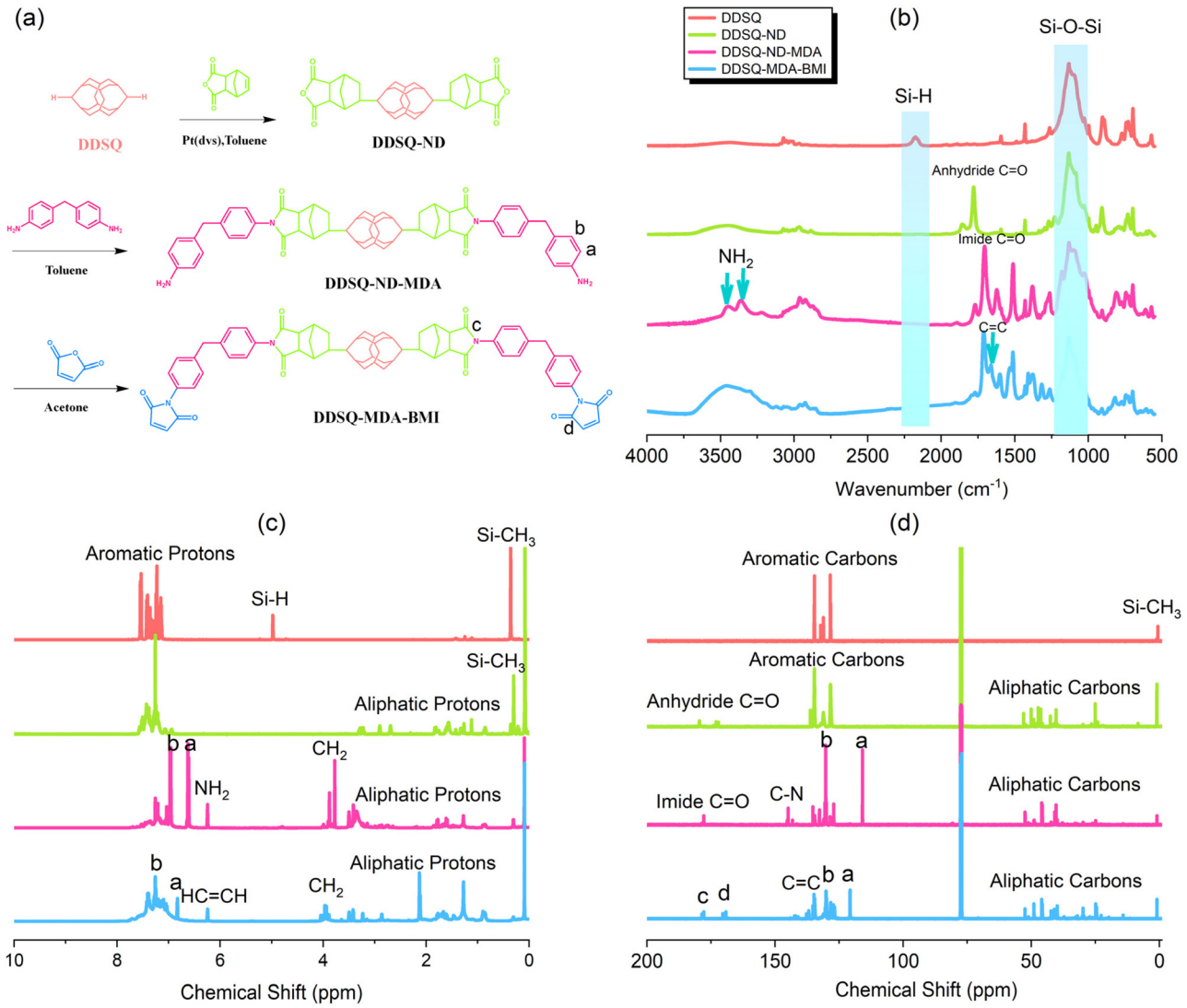

Fig. 1 (a) Synthesis of **DDSQ-MDA-BMI** from **DDSQ**, **DDSQ-ND** and **DDSQ-ND-MDA**, and each corresponding (b) FTIR, (c) ^{1}H NMR and (d) ^{13}C NMR spectra.

condenser. Toluene (60 mL) was added drop by drop, and the solution was stirred, then heated to 105 °C for 48 h under a blanket of N_2. The solution was removed by rotary distillation under vacuum. After it was placed in a vacuum oven, it was heated at 180 °C for 36 h to obtain a brownish yellow or black solid product, with a yield of 86% for **DDSQ-ND-MDA** and 88% for **DDSQ-ND-MPD**.

Synthesis of DDSQ-MDA-BMI and DDSQ-MPD-BMI

DDSQ-ND-MDA (7.37 g, 4 mmol) or **DDSQ-ND-MPD** (6.65 g, 4 mmol) and excess maleic anhydride (0.83 g, 82 mmol) were placed into a flask covered with N_2. Next, 70 mL of dry acetone was added dropwise with vigorous stirring until dissolution. In addition, 60 mL of dry acetone was placed into a beaker containing maleic anhydride and stirred until dissolution. The maleic anhydride solution was added to the flask *via* a titration funnel, and the flask was agitated for 1 h. The mixture was heated to 40 °C and maintained at that temperature for an additional 30 min. Acetic anhydride (2.83 mL, 30 mmol) and *N*,*N*-diethylethanamine (0.56 mL, 4 mmol) were subsequently added to the flask. Unreacted solids were removed by filtration after 48 h.

The crude product was dripped into a 1000 mL beaker filled with ice and deionized water, quickly stirred, and the stirring was stopped so that precipitation could proceed. The precipitate was filtered and washed with 10% sodium carbonate. The product was placed in a vacuum oven at room temperature for 1 day. The resultant compounds are referred to as **DDSQ-MDA-BMI** (light yellow, yield: 78%) and **DDSQ-MPD-BMI** (black, yield: 81%).

Preparation of cured DDSQ-BMI resins

DDSQ-BMI powder was placed in an aluminium dish for curing in an oven under air. The curing cycles of DDSQ-BMI

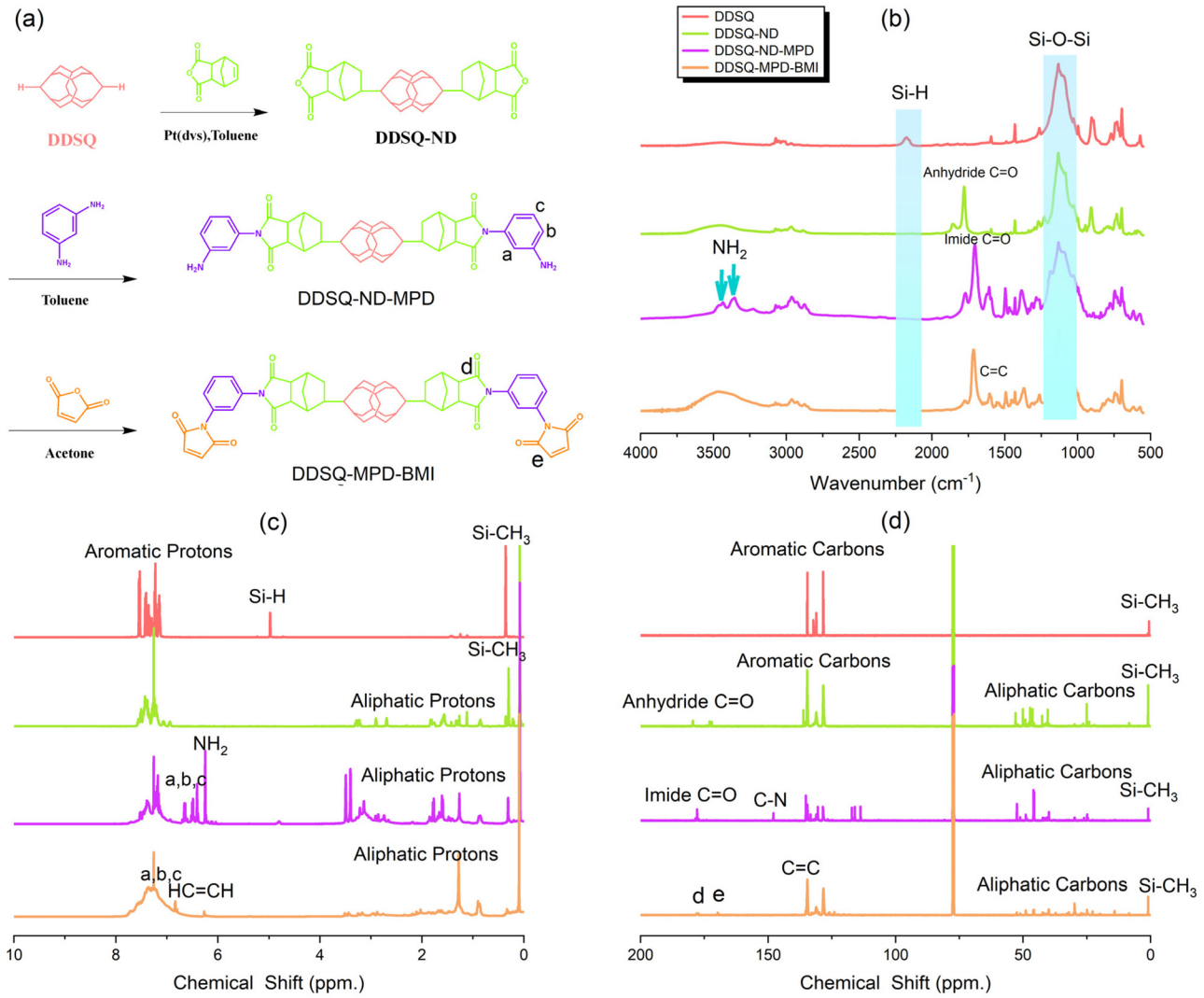

Fig. 2 (a) Synthesis of **DDSQ-MPD-BMI** from **DDSQ**, **DDSQ-ND** and **DDSQ-ND-MPD**, and each corresponding (b) FTIR, (c) ^{1}H NMR and (d) ^{13}C NMR spectra.

were as follows: 2 h at 240 °C, 2 h at 320 °C, 2 h at 400 °C, 2 h at 480 °C, and 2 h at 520 °C. The powders were removed from the oven at each temperature. The cured resins are referred to as c-**DDSQ-MDA-BMI** and c-**DDSQ-MPD-BMI**.

Results and discussion

MDA-BMI and MPD-BMI were examined by ^{1}H NMR and FTIR spectroscopy. In the spectra of MDA-BMI as displayed in Fig. S1(a) and (c),† the aromatic protons were distributed at 7.12–7.39 ppm, and the CH_2 unit appeared at 3.85 ppm. The vinyl signals for maleic anhydride units were at 7.63 ppm. Because the signals of the C═O bonds could not be observed by ^{1}H NMR, two peaks at 1707 and 1762 cm^{-1} were identified by FTIR. For MPD-BMI (Fig. S1(b) and (d)†), signals of aromatic protons appeared at 6.27, 7.22, and 7.35 ppm, and the vinyl signals for maleic anhydride units appeared at 8.09 ppm. Two signals at 1695 and 1783 cm^{-1} were observed for MPD-BMI, which was confirmed by FTIR.

Fig. 1(a) and 2(a) show the synthesis scheme for **DDSQ-MDA-BMI** and **DDSQ-MPD-BMI**, respectively. Each intermediate chemical structure from **DDSQ** to DDSQ-BMI products was confirmed by FTIR, ^{1}H NMR and ^{13}C NMR analysis. Fig. 1(b) and 2(b) display the FTIR spectra, and there was a Si–CH_3 signal at 1264 cm^{-1} and Si–O–Si signal at 1132 cm^{-1} for all **DDSQ** derivatives. Through hydrosilylation by **DDSQ** with ND, the Si–H absorption bands at 2182 cm^{-1} disappeared and formed doublet peaks at 1857 and 1780 cm^{-1} by anhydride C═O units. **DDSQ-ND-MDA** and **DDSQ-ND-MPD** have imide groups attached to MDA and MPD through **DDSQ-ND**.

Therefore, the imide C═O units of **DDSQ-ND-MDA** resulted in two absorptions at 1705 and 1770 cm^{-1}, while the imide C═O units of **DDSQ-ND-MPD** were at 1706 and 1771 cm^{-1}. They also produced two signals corresponding to symmetric and asymmetric NH_2 units: **DDSQ-ND-MDA** was at 3366 and 3454 cm^{-1}, and **DDSQ-ND-MPD** was at 3354 and 3435 cm^{-1}, respectively. After the formation of DDSQ-BMI products, the signals of the NH_2 units disappeared, and the imide C═O units of **DDSQ-MDA-BMI** were slightly red-shifted to 1712 and 1771 cm^{-1}, while **DDSQ-MPD-BMI** was also slightly red-shifted to 1715 and 1778 cm^{-1}.

Fig. 1(c) and 2(c) display the **DDSQ** derivative spectra of the ^{1}H NMR analysis. For **DDSQ** derivatives, several signals at 6.8 to 7.6 ppm were obtained for the aromatic protons of **DDSQ**, and one signal at 0.38 ppm for Si–CH_3. Through hydrosilylation by **DDSQ** with ND, there were some peaks at 0.87 ppm to 3.55 ppm by aliphatic protons with two isomers, and the Si–H proton signal at 4.98 ppm disappeared.[41] For **DDSQ-ND-MDA** and **DDSQ-ND-MPD**, the spectra of ^{1}H NMR displayed a broad peak at 3.36 and 3.14 ppm for the NH_2 unit, respectively, and four peaks at 6.24 to 6.65 ppm for the aromatic protons of MDA or MPD units. When DDSQ-BMI products are formed, the NH_2 signal will disappear, and the double bond signals of the MA units will be generated at 6.82 ppm. Fig. 1(d) and 2(d) show the **DDSQ** derivative spectra for the ^{13}C NMR analysis. All

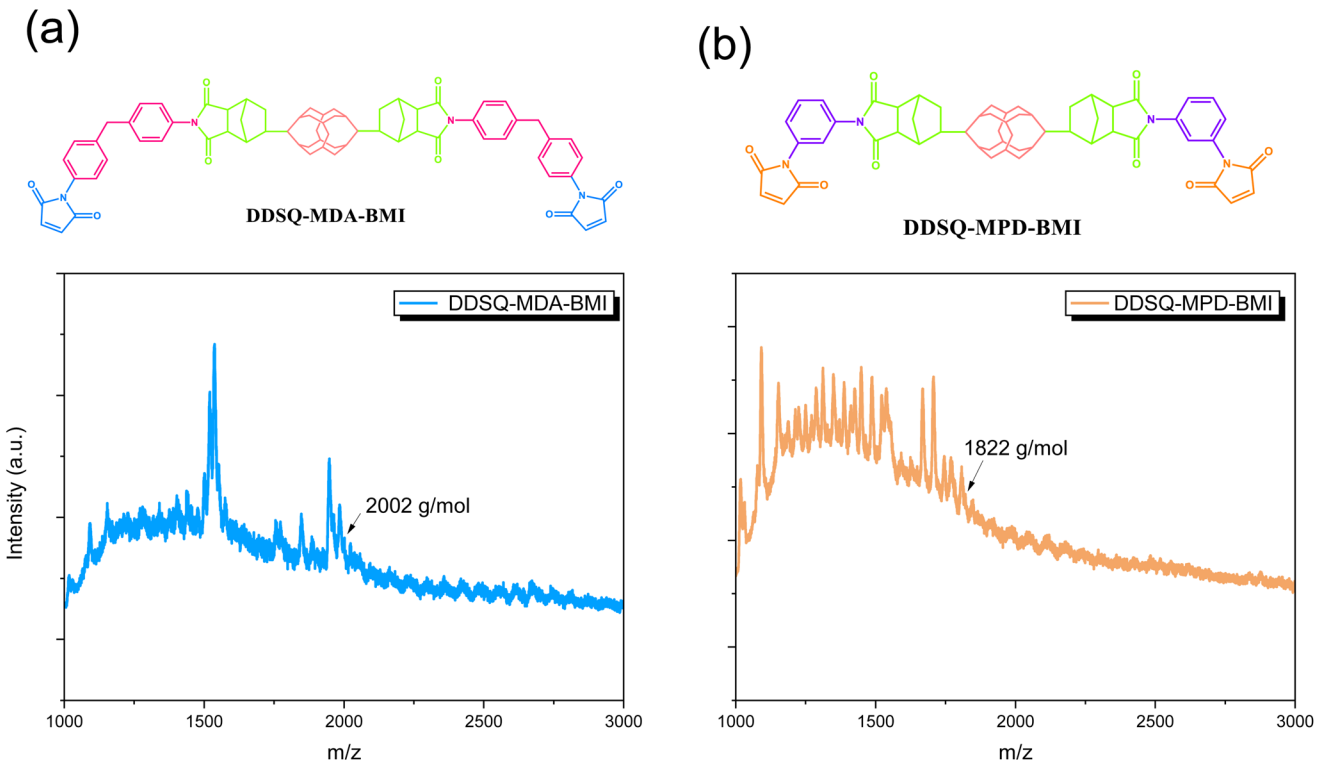

Fig. 3 MALDI-TOF mass spectra of (a) **DDSQ-MDA-BMI** and (b) **DDSQ-MPD-BMI**.

DDSQ derivatives exhibited one signal for Si–CH_3 at 1.0 ppm and many signals for the aromatic carbons of **DDSQ** from 128 to 134 ppm.

After hydrosilylation to form **DDSQ-ND**, signals of aliphatic carbons at 25 to 52 ppm and anhydride C═O at 179 ppm appeared. For **DDSQ-ND-MDA**, new signals appeared at 177 ppm (imide C═O), 144 ppm (C–N), 115 ppm (***a*** from the MDA aromatic), and 130 ppm (***b*** from the MDA aromatic). Similarly, at 177 ppm (imide C═O), 147 ppm (C–N), 113 ppm (***a*** from the MPD aromatic), and 128 ppm (***b*** from the MPD aromatic), novel signals for **DDSQ-ND-MPD** were observed. Finally, the C═C signal from the MA units will be produced at 134 ppm when DDSQ-BMI products are synthesized. There are two C═O signals for ND units at 177 and 178 ppm, and there are also two C═O signals for MA units at 169 and 170 ppm. Fig. 3 shows the MALDI-TOF mass spectra of DDSQ-BMI final products. Many different signals were generated due to the fragments of different sizes that were generated after exposure of the sample to the laser. However, the signal belonging to **DDSQ-MDA-BMI** and **DDSQ-MPD-BMI** appeared at 2002 g mol^{-1} and 1822 g mol^{-1}, respectively. Based on the FTIR, NMR, and MALDI-TOF mass spectra analyses, it was concluded that **DDSQ-MDA-BMI** and **DDSQ-MPD-BMI** were successfully synthesized in this study.

Fig. 4(a) and (b) present the DSC thermograms of **DDSQ-MDA-BMI** and **DDSQ-MPD-BMI**, with heating rates of 20 °C min^{-1}. The small endothermic peak at 168 °C (enthalpy of −6.06 J g^{-1}) and obvious broad exothermic peak at 234 °C (enthalpy of 37.50 J g^{-1}) correspond to the pure **DDSQ-MDA-BMI** melting temperature and additional polymerization process, respectively. Similarly, the melting temperature of **DDSQ-MPD-BMI** was at 75 °C (enthalpy of −2.67 J g^{-1}), and the exothermic peak at 262 °C (enthalpy of 29.58 J g^{-1}) was due to additional polymerization. The thermal curing products (c-**DDSQ-MDA-BMI** and c-**DDSQ-MPD-BMI**) underwent TGA analyses from room temperature to 800 °C at a heating rate of 20 °C min^{-1}, as displayed in Fig. 4(c) and (d). The temperature at 10% weight loss ($T_{d\,10}$) and char yield of c-**DDSQ-MDA-BMI** were 300 °C and 40.98 wt%, respectively. Both values increased with increasing thermal curing tempera-

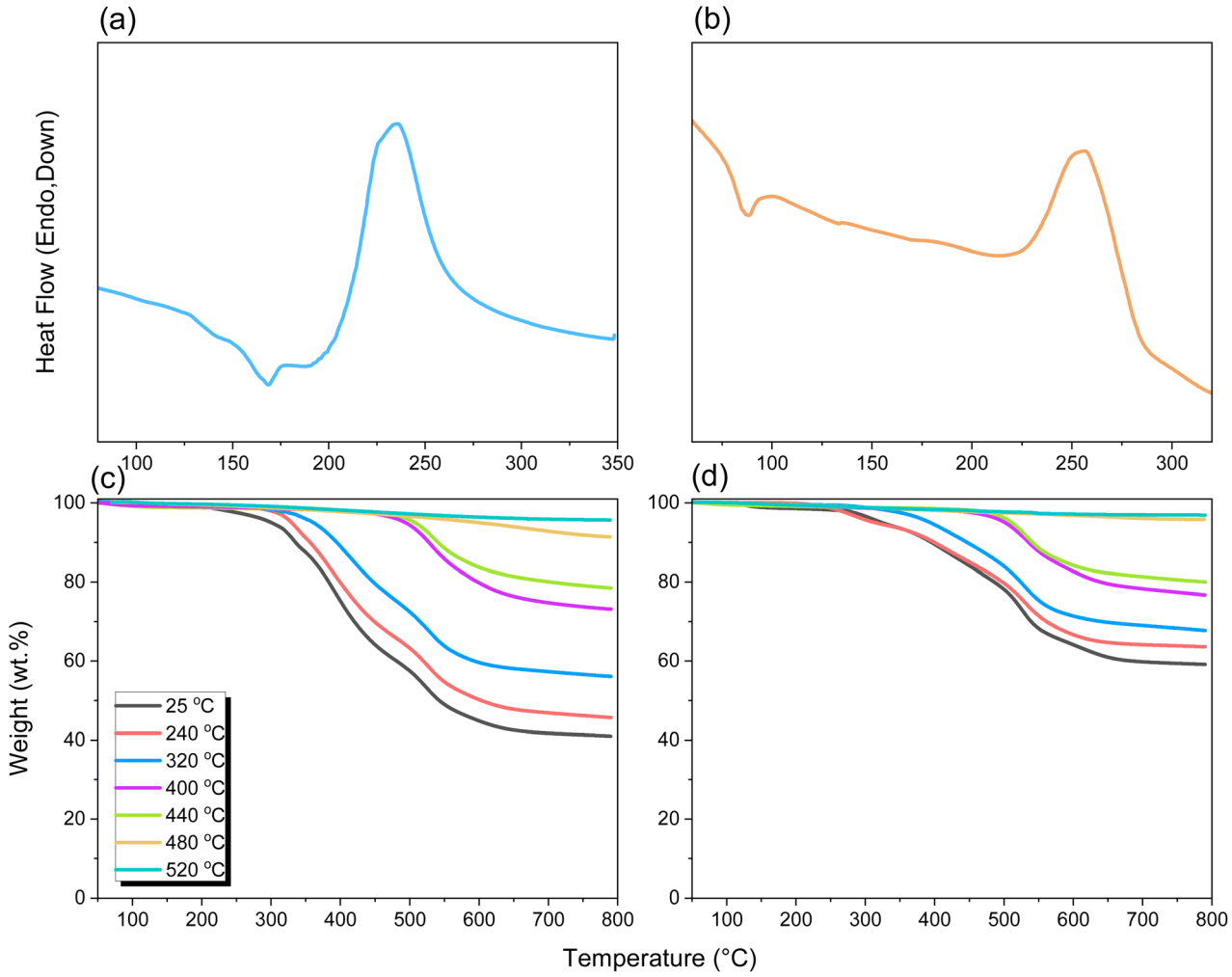

Fig. 4 DSC analyses of (a) **DDSQ-MDA-BMI** and (b) **DDSQ-MPD-BMI** from the first heating run. TGA analyses of (c) c-**DDSQ-MDA-BMI** and (d) c-**DDSQ-MPD-BMI** at each thermal curing temperature.

ture. When the thermal curing temperature was 520 °C, the char yield reached 95.68 wt%. Similarly, the $T_{d\,10}$ value of c-**DDSQ-MPD-BMI** was 324 °C, and the char yield value increased from 59.14 wt% to 96.04 wt% upon increasing the thermal curing temperature. When the thermal curing temperature was 480 °C, no thermal degradation occurred due to the formation of a cross-linked structure.[35,36]

Fig. 5 displays the corresponding FTIR spectra of c-DDSQ-BMI products that underwent various thermal curing temperatures. The signal at 1132 cm^{-1} for Si–O–Si bonds did not disappear under high-temperature thermal curing due to the cage structure of the inorganic **DDSQ** nanoparticles. In contrast, the signals of the C═O units for **DDSQ-MDA-BMI** (at 1713 and 1770 cm^{-1}) and **DDSQ-MPD-BMI** (at 1716 and 1780 cm^{-1}) all decreased after thermal curing at 520 °C. At a curing temperature of 400 °C, the maleic anhydride units will undergo double bond cleavage, which will then transform into a single bond, forming an aliphatic.[35,36] However, as the curing temperature further increases to 520 °C, the C–H and C–C bonds for the aliphatic will be destroyed, resulting in the signals at 2850–2927 cm^{-1} initially increasing and then weakening. The signals of the aromatic CH at 1645 and 1634 cm^{-1} did not change after thermal curing.

We obtained N_2 isotherm adsorption curves to confirm the pore sizes and specific surface areas of c-DDSQ-BMI products after thermal curing (Fig. 6). The adsorption and desorption curves overlapped, which indicated that the material exhibits uniform adsorption and desorption without any observable hysteresis. For c-**DDSQ-MDA-BMI** heated at 480 °C for 6 h, the surface area was 826 $m^2\ g^{-1}$ (Table 1), which was the greatest in contrast to the samples heated to 480 °C for 4 h (411 $m^2\ g^{-1}$) and 520 °C for 4 h (557 $m^2\ g^{-1}$). Similarly, the surface area of c-**DDSQ-MPD-BMI** heated at 480 °C for 6 h (352 $m^2\ g^{-1}$) was greater than that heated at 480 °C for 4 h (222 $m^2\ g^{-1}$) and 520 °C for 4 h (109 $m^2\ g^{-1}$). In addition, the average pore width was 2.28–3.39 nm, which conforms to a mesoporous morphology.

TEM images were used to observe the porous distribution. Fig. 7(a and b) shows c-**DDSQ-MDA-BMI** at 480 °C for 4 h and 6 h, respectively, and Fig. 7(d and e) shows c-**DDSQ-MPD-BMI**

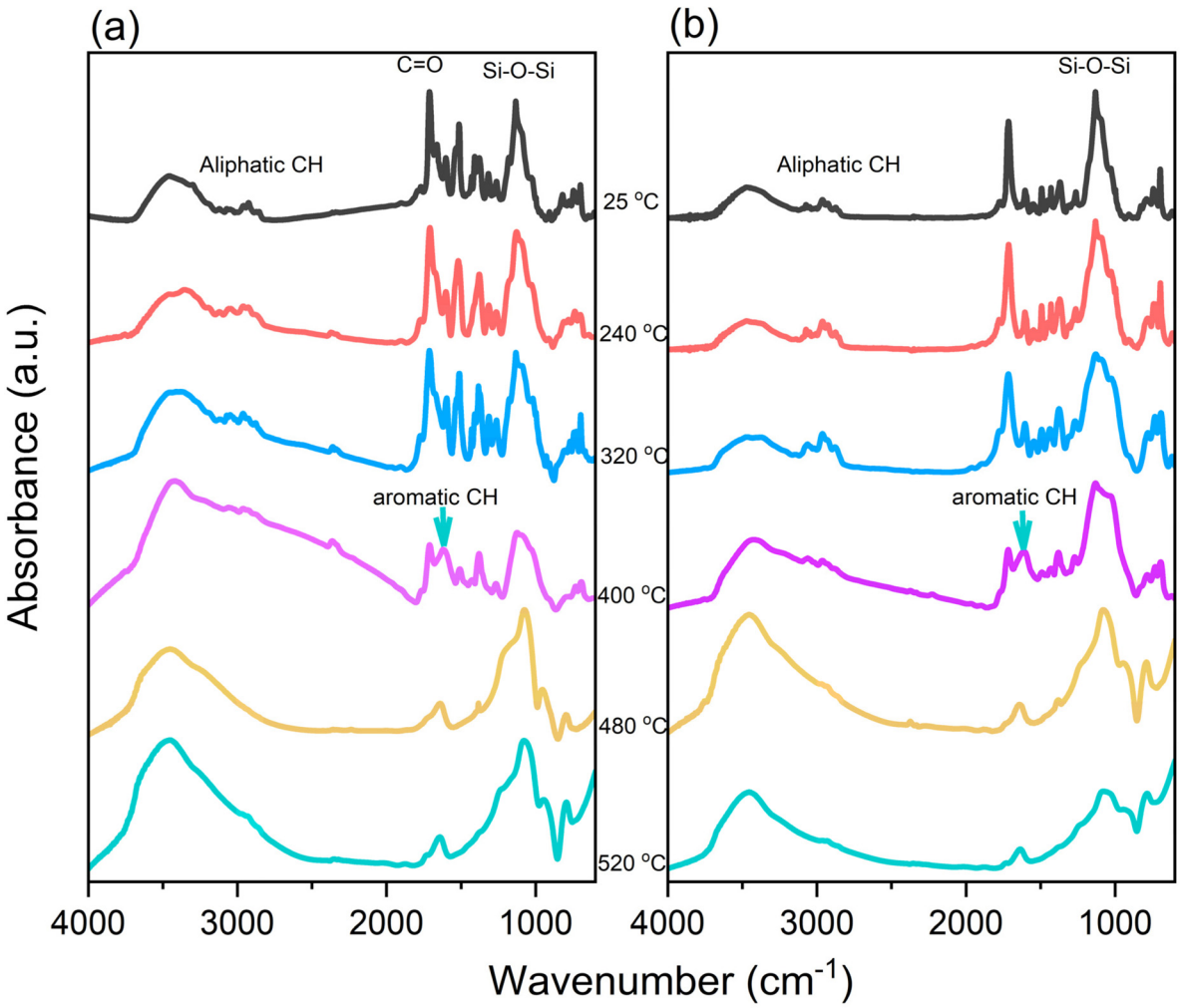

Fig. 5 FTIR spectra of (a) c-**DDSQ-MDA-BMI** and (b) c-**DDSQ-MPD-BMI** at each thermal curing temperatures.

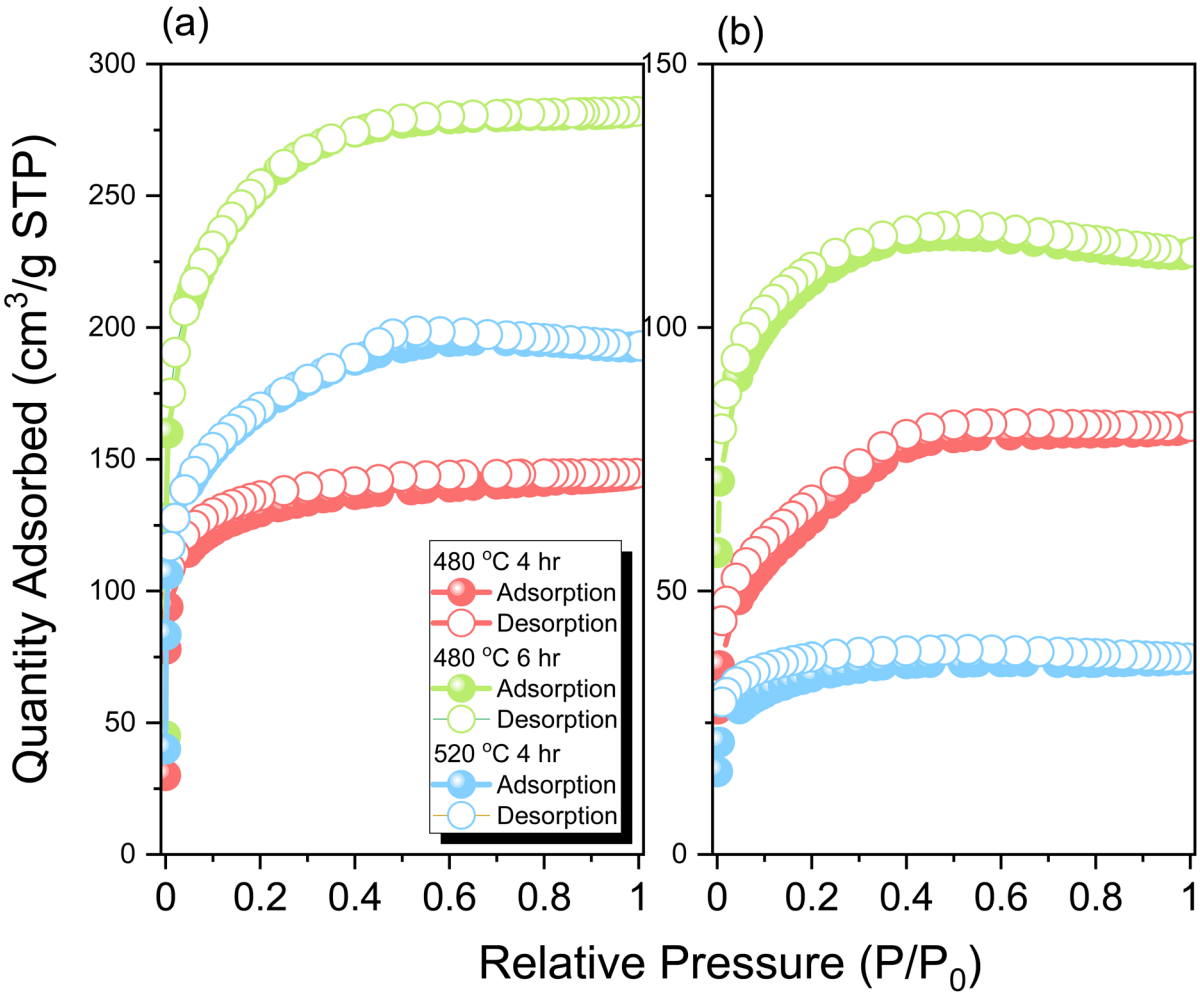

Fig. 6 N_2 adsorption/desorption isotherms of (a) c-**DDSQ-MDA-BMI** and (b) c-**DDSQ-MPD-BMI** with different thermal curing procedures at 480 °C for 4 h, 480 °C for 6 h and 520 °C for 4 h.

Table 1 BET surface areas and pore properties of c-**DDSQ-MDA-BMI** and c-**DDSQ-MPD-BMI**

	c-**DDSQ-MDA-BMI**			c-**DDSQ-MPD-BMI**		
Sample	480 °C/4 h	480 °C/6 h	520 °C/4 h	480 °C/4 h	480 °C/6 h	520 °C/4 h
Surface area (m^2 g^{-1})	411	826	557	222	352	109
$S_{microporous}$ (m^2 g^{-1})	252	324	212	32	158	44
Pore volume (cm^3 g^{-1})	0.135	0.164	0.166	0.09	0.496	0.016
Average pore size (nm)	4.19	2.84	2.33	2.52	3.21	3.56

at 480 °C for 4 h and 6 h, respectively. We found that some pores were distributed on the surface of the material in all of the figures. This proves that our c-DDSQ-BMI products successfully crosslinked to form a porous structure. In addition, Fig. 7(c) and (f) shows the EDS images of c-**DDSQ-MDA-BMI** and c-**DDSQ-MPD-BMI**, respectively, and these were used to confirm the ratio of Si, C, and O atoms, as summarized in Table S1.†

The CO_2 adsorption isotherms of c-DDSQ-BMI products heated at 480 °C for 6 h were measured at 273 K and 298 K, as displayed in Fig. 8. c-**DDSQ-MDA-BMI** exhibited the highest CO_2 adsorption capacity of 38.95 cm^3 g^{-1} STP (7.71 wt%) at 273 K and 1 bar due to the high surface area and large amounts of N units. Compared with c-**DDSQ-MDA-BMI**, there is relatively less adsorption capacity for c-**DDSQ-MPD-BMI** at 8.73 cm^3 g^{-1} STP (1.73 wt%). These modified units increased their capacity to collect CO_2 through [N···C═O] acid–base interactions. Furthermore, the isosteric enthalpies (Q_{st}) of c-DDSQ-BMI products were determined using the Clausius–Clapeyron equation. The Q_{st} values of c-**DDSQ-MDA-BMI** and c-**DDSQ-MPD-BMI** were 20.84 and 15.06 kJ mol^{-1}, respectively,

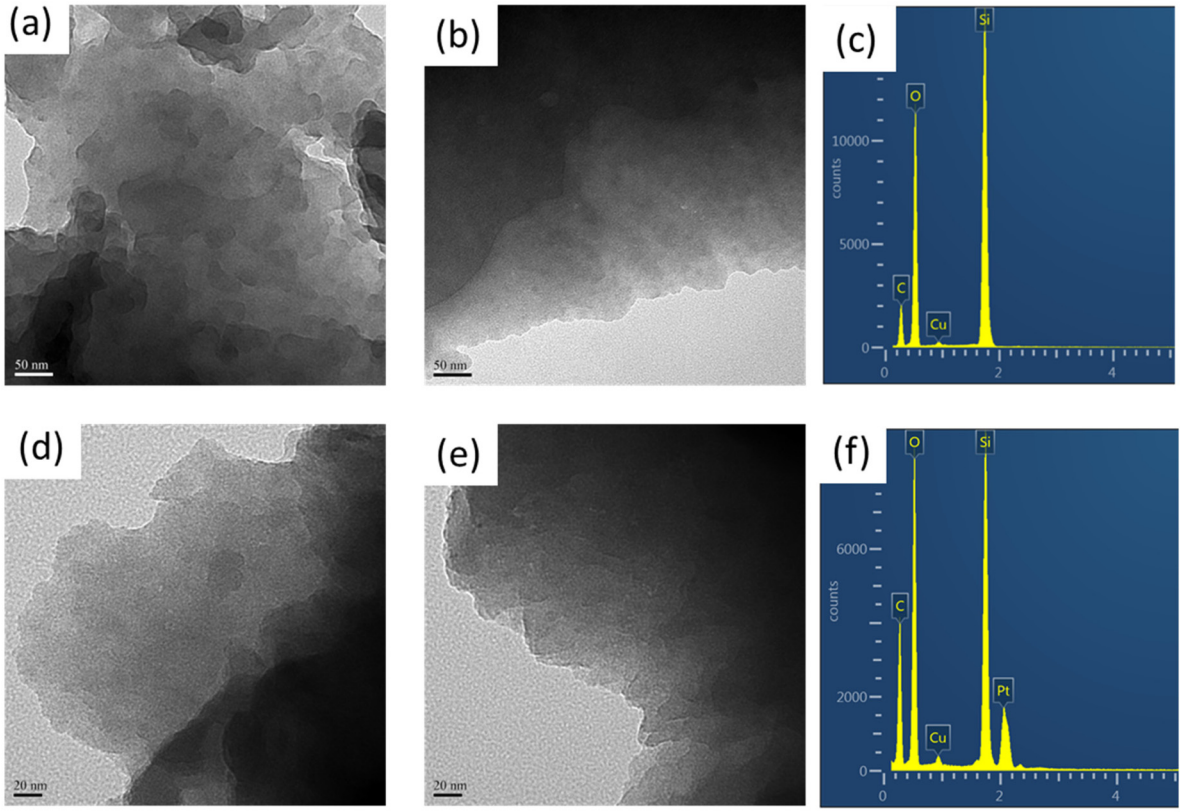

Fig. 7 TEM images of samples after they underwent thermal curing at 480 °C for 4 h and at 480 °C for 6 h with (a and b) c-**DDSQ-MDA-BMI** and (d and e) c-**DDSQ-MPD-BMI**. EDS image for (c) c-**DDSQ-MDA-BMI** and (f) c-**DDSQ-MPD-BMI**.

at high CO_2 adsorption (approximately 8.1 $cm^3\ g^{-1}$ STP). The Q_{st} value for c-**DDSQ-MDA-BMI** was much higher than that for c-**DDSQ-MPD-BMI** because of the higher surface area and pore volume of the former.

The cyclic voltammetry (CV) and the galvanostatic charge discharge (GCD) methods were used to examine the electrochemical performance of c-DDSQ-BMI products after thermal curing at 480 °C for 6 h. We used a three-electrode setup con-

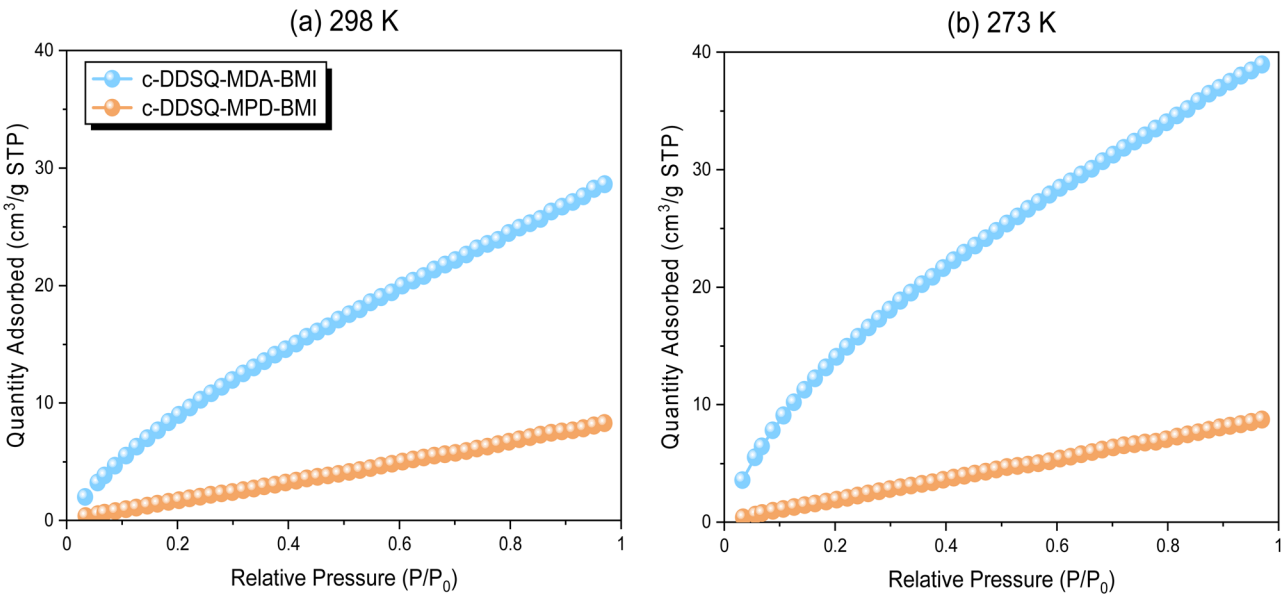

Fig. 8 CO_2 uptake at (a) 298 K and (b) 273 K by c-**DDSQ-MDA-BMI** and c-**DDSQ-MPD-BMI** after thermal curing at 480 °C for 6 h.

sisting of glassy carbon, platinum wire, and Hg/HgO as the working, counter, and reference electrodes, respectively and placed them in 1 M aqueous KOH. We measured the CV traces at various scan rates from 5 to 200 mV s^{-1} over a potential range from −1 to 0 V, as shown in Fig. 9(a) and (c). There are oxidation peaks at −0.35 V and −0.49 V for c-**DDSQ-MDA-BMI** and c-**DDSQ-MPD-BMI**, respectively.

The reduction peaks of the two c-DDSQ-BMI products are not seen in the range of −1 to 0 V because the oxidation peak is not symmetrical with the reduction peak.

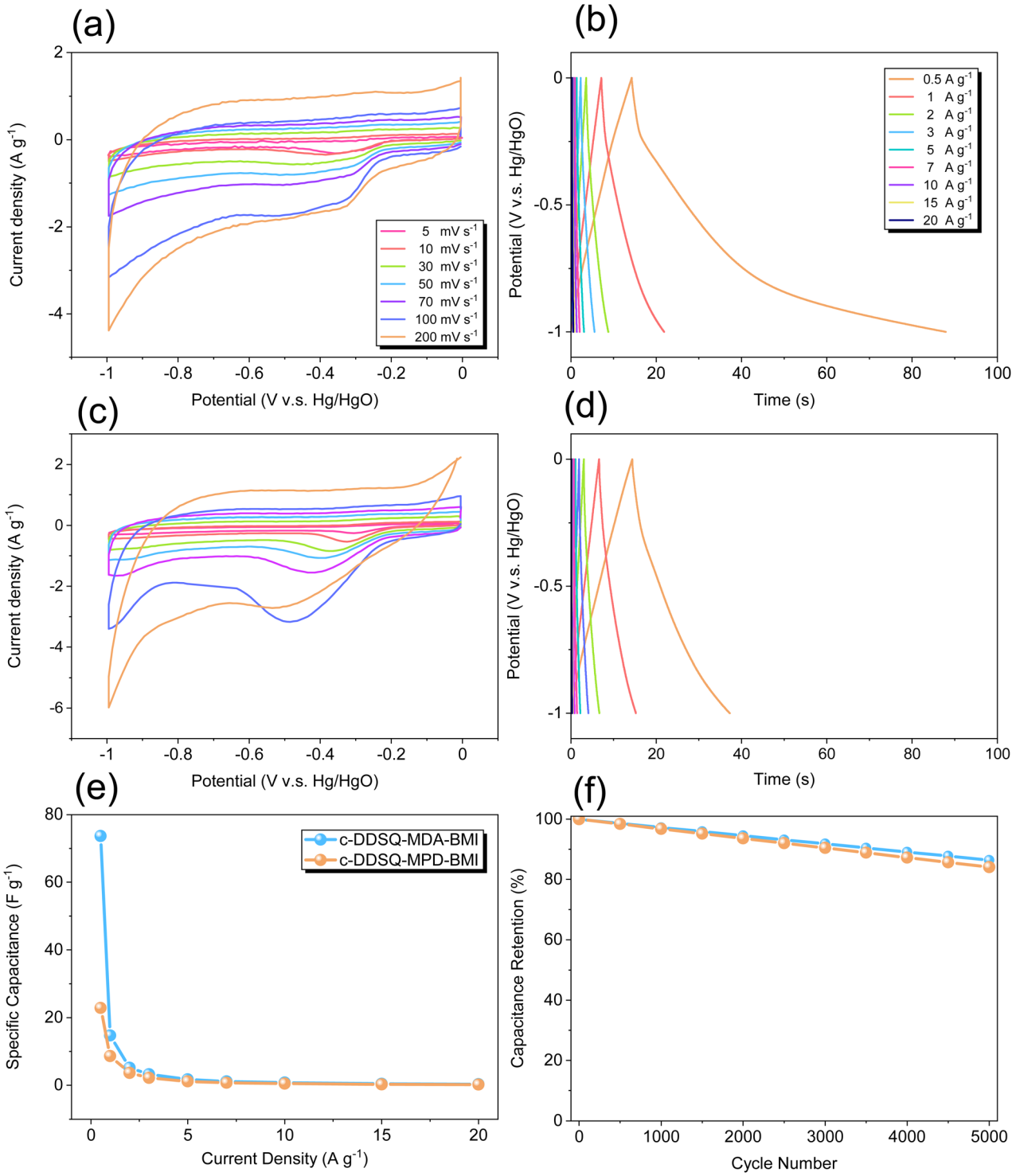

Fig. 9 Electrochemical performance of CV, and GCD analyses with (a and c) c-**DDSQ-MDA-BMI** and (b and d) c-**DDSQ-MPD-BMI** after thermal curing at 480 °C for 6 h; (e) capacitance and (f) capacitance retention.

Furthermore, we measured the capacitance of these compounds at current densities ranging from 0.5 to 20 A g^{-1}, as shown in Fig. 9(b) and (d). There is a longer discharge time for c-**DDSQ-MDA-BMI** as compared to c-**DDSQ-MPD-BMI**, indicating a higher specific capacitance. The specific capacitance of c-**DDSQ-MDA-BMI** and c-**DDSQ-MPD-BMI** at 0.5 A g^{-1} was 73.66 and 22.86 F g^{-1}, respectively, as shown in Fig. 9(e). As the current density increased, the specific capacitance of c-**DDSQ-MDA-BMI** tended to be equivalent to that of c-**DDSQ-MPD-BMI**.

Fig. 9(f) further demonstrates the long-term cycling stability of our c-DDSQ-BMI products, with capacitance retentions of 86.4% and 84.1%, respectively, for 5000 cycles at 10 A g^{-1}. Table S2† presents a performance analysis of c-**DDSQ-MDA-BMI** and c-**DDSQ-MPD-BMI** as organic electrodes in SC applications compared to other porous electrode materials.

Conclusions

We synthesized DDSQ-BMI products through multi-step chemical reactions and confirmed their successful synthesis through FTIR and NMR spectroscopy, as well as MALDI-TOF. There was a higher $T_{d\,10}$ value (324 °C) and char yield (59.14 wt%) for **DDSQ-MPD-BMI**. All values increased after thermal curing at different thermal temperatures. In addition, the TEM images show pores distributed on the surface of DDSQ-BMI products. Using N_2 adsorption/desorption isotherms, we determined that a high surface area (826 m^2 g^{-1}) with high porosity was formed on c-**DDSQ-MDA-BMI** after thermal curing at 480 °C for 6 h. Therefore, we used this porous material to analyze the CO_2 absorption and electrochemical performance of c-**DDSQ-MDA-BMI**, which exhibited excellent CO_2 adsorption (38.95 cm^3 g^{-1} STP), specific capacitance (73.66 F g^{-1}), and capacitance retention (86.4%). These data reveal that c-DDSQ-BMI products are porous materials that can efficiently store and separate gases without a catalyst and can undergo carbonization at high temperatures (>600 °C).

Author contributions

Zih-Yu Chen: investigation, methodology, conceptualization, supervision, writing – original draft. Wei-Cheng Chen: investigation, methodology, writing – original draft. Shiao-Wei Kuo: supervision and writing.

Conflicts of interest

There are no conflicts to declare.

Acknowledgements

This study was financially supported by the National Science and Technology Council, Taiwan, under contracts NSTC 112-2218-E-110-007 and 112-2223-E-110-002. The authors thank the staff at National Sun Yat-sen University for their assistance with the TEM (ID: EM022600) experiments.

References

1 D. H. Yang, Y. Tao, X. Ding and B. H. Han, Porous Organic Polymers for Electrocatalysis, *Chem. Soc. Rev.*, 2022, **51**, 761–791.
2 L. Chen, C. Gong, X. Wang, F. Dai, M. Huang, X. Wu, C. Z. Lu and Y. Peng, Substoichiometric 3D Covalent Organic Frameworks Based on Hexagonal Linkers, *J. Am. Chem. Soc.*, 2021, **143**, 10243–10249.
3 H. Wang, Y. Jin, N. Sun, W. Zhang and J. Jiang, Post-Synthetic Modification of Porous Organic Cages, *Chem. Soc. Rev.*, 2021, **50**, 8874–8886.
4 X. Zhang, J. Maddock, T. M. Nenoff, M. A. Denecke, S. Yang and M. Schröder, Adsorption of iodine in metal-organic framework materials, *Chem. Soc. Rev.*, 2022, **51**, 3243–3262.
5 P. Kaur, J. T. Hupp and S. T. Nguyen, Porous Organic Polymers in Catalysis: Opportunities and Challenges, *ACS Catal.*, 2011, **1**, 819–835.
6 M. G. Mohamed, H. Y. Hu, M. Madhu, M. M. Samy, I. M. A. Mekhemer, W. T. Tseng, H. H. Chou and S. W. Kuo, Ultrastable two-dimensional fluorescent conjugated microporous polymers containing pyrene and fluorene units for metal ion sensing and energy storage, *Eur. Polym. J.*, 2023, **189**, 111980.
7 M. Ejaz, M. G. Mohamed and S. W. Kuo, Solid state chemical transformation provides a fully benzoxazine-linked porous organic polymer displaying enhanced CO_2 capture and supercapacitor performance, *Polym. Chem.*, 2023, **14**, 2494–2509.
8 M. G. Mohamed, S. Y. Chang, M. Ejaz, M. M. Samy, A. O. Mousa and S. W. Kuo, Design and Synthesis of Bisulfone-Linked Two-Dimensional Conjugated Microporous Polymers for CO_2 Adsorption and Energy Storage, *Molecules*, 2023, **28**, 3234.
9 A. O. Mousa, I. L. Zheng, C. H. Chuang, C. K. Chen, S. W. Kuo and M. G. Mohamed, Rational Design of Bifunctional Microporous Organic Polymers Containing Anthracene and Triphenylamine Units for Energy Storage and Biological Applications, *Int. J. Mol. Sci.*, 2023, **24**, 8966.
10 M. M. Samy, I. M. A. Mekhemer, M. G. Mohamed, M. H. Elsayed, K. H. Lin, Y. K. Chen, T. L. Wu, H. H. Chou and S. W. Kuo, Conjugated microporous polymers incorporating Thiazolo[5,4-d]thiazole moieties for Sunlight-Driven hydrogen production from water, *Chem. Eng. J.*, 2022, **446**, 137158.

11 Y. Zhu, P. Xu, X. Zhang and D. Wu, Emerging porous organic polymers for biomedical applications, *Chem. Soc. Rev.*, 2022, **51**, 1377–1414.
12 M. G. Mohamed, A. F. M. El-Mahdy, M. G. Kotp and S. W. Kuo, Advances in porous organic polymers: syntheses, structures, and diverse applications, *Mater. Adv.*, 2022, **3**, 707–733.
13 Y. Yuan and G. Zhu, Porous aromatic frameworks as a platform for multifunctional applications, *ACS Cent. Sci.*, 2019, **5**, 409–418.
14 T. Zhang, G. Xing, W. Chen and L. Chen, Porous organic polymers: a promising platform for efficient photocatalysis, *Mater. Chem. Front.*, 2020, **4**, 332–353.
15 Y. Yuan and G. Zhu, Porous aromatic frameworks as a platform for multifunctional applications, *ACS Cent. Sci.*, 2019, **5**, 409–418.
16 H. R. Abuzeid, A. F. M. El-Mahdy and S. W. Kuo, Covalent Organic Frameworks: Design Principles, Synthetic Strategies, and Diverse Applications, *Giant*, 2021, **6**, 100054.
17 M. Kim, R. Xin, J. Earnshaw, J. Tang, J. P. Hill, A. Ashok, A. K. Nanjundan, J. Kim, C. Young, Y. Sugahara, J. Na and Y. Yamauchi, MOF-Derived Nanoporous Carbons with Diverse Tunable Nanoarchitectures, *Nat. Protoc.*, 2022, **17**, 2990–3027.
18 X. Chen, M. Addicoat, E. Jin, L. Zhai, H. Xu, N. Huang, Z. Guo, L. Liu, S. Irle and D. Jiang, Locking Covalent Organic Frameworks with Hydrogen Bonds: General and Remarkable Effects on Crystalline Structure, Physical Properties, and Photochemical Activity, *J. Am. Chem. Soc.*, 2015, **137**, 3241–3247.
19 S. W. Kuo, Construction Archimedean tiling patterns based on soft materials from block copolymers and covalent organic frameworks, *Giant*, 2023, **15**, 100170.
20 W. T. Chung, I. M. A. Mekhemer, M. G. Mohamed, A. M. Elewa, A. F. M. El-Mahdy, H. H. Chou, S. W. Kuo and K. C. W. Wu, Recent advances in metal/covalent organic frameworks based materials: Their synthesis, structure design and potential applications for hydrogen production, *Coord. Chem. Rev.*, 2023, **483**, 215066.
21 F. Begni, F. Gullo, G. Paul, R. Rea, M. C. Ferrari, E. Mangano, M. Cossi, G. Gatti and L. Marchese, Optimization of the Friedel–Crafts Alkylation for the Synthesis of Hyper-Cross-Linked Polymers, *ACS Appl. Polym. Mater.*, 2022, **4**, 5281–5286.
22 L. Pan, Q. Chen, J. H. Zhu, J. G. Yu, Y. J. He and B. H. Han, Hypercrosslinked Porous Polycarbazoles via One-Step Oxidative Coupling Reaction and Friedel–Crafts Alkylation, *Polym. Chem.*, 2015, **6**, 2478–2487.
23 H. Gao, L. Ding, W. Li, G. Ma, H. Bai and L. Li, Hyper-Cross-Linked Organic Microporous Polymers Based on Alternating Copolymerization of Bismaleimide, *ACS Macro Lett.*, 2016, **5**, 377–381.
24 J. Huang and R. Turner, Hypercrosslinked Polymers: A Review, *Polym. Rev.*, 2018, **58**, 1–41.
25 T. Zhu, Q. Yu, L. Ding, T. Di, T. Zhao, T. Li and L. Li, Atom-economical preparation of polybismaleimide-based microporous organic polymers, *Green Chem.*, 2019, **21**, 2326–2333.
26 R. J. Iredale, C. Ward and I. Hamerton, Modern advances in bismaleimide resin technology: A 21st century perspective on the chemistry of addition polyimides, *Prog. Polym. Sci.*, 2017, **69**, 1–21.
27 A. Gu, High Performance Bismaleimide/cyanate Ester Hybrid Polymer Networks with Excellent Dielectric Properties, *Compos. Sci. Technol.*, 2006, **66**, 1749–1755.
28 X. Li, Y. Zhou, Y. Bao, W. Wei, X. Fei, X. Li and X. Liu, Bismaleimide/Phenolic/Epoxy Ternary Resin System for Molding Compounds in High-Temperature Electronic Packaging Applications, *Ind. Eng. Chem. Res.*, 2022, **61**, 4191–4201.
29 W. Guo, F. Liang, S. Chen, D. Zhang, W. Li, K. Qian, Y. Xu and B. Fei, Synthesis of magnolol-derived bisphosphate for fabrication of bismaleimide resins with intrinsic anti-flammability and smoke suppression, *Polym. Degrad. Stab.*, 2022, **202**, 110002.
30 W. Wang, M. Zhou and D. Yuan, Carbon Dioxide Capture in Amorphous Porous Organic Polymers, *J. Mater. Chem. A*, 2017, **5**, 1334–1347.
31 C. Xu and N. Hedin, Microporous Adsorbents for CO_2 Capture – a Case for Microporous Polymers?, *Mater. Today*, 2014, **17**, 397–403.
32 M. G. Mohamed, S. Y. Chang, M. Ejaz, M. M. Samy, A. O. Mousa and S. W. Kuo, Design and Synthesis of Bisulfone-Linked Two-Dimensional Conjugated Microporous Polymers for CO_2 Adsorption and Energy Storage, *Molecules*, 2023, **28**, 3234.
33 M. M. Samy, M. G. Mohamed and S. W. Kuo, Conjugated Microporous Polymers Based on Ferrocene Units as Highly Efficient Electrodes for Energy Storage, *Polymers*, 2023, **15**, 1095.
34 W. C. Chen, Z. Y. Chen, Y. Ba, B. Wang, G. Chen, X. Fang and S. W. Kuo, Double-Decker-Shaped Polyhedral Silsesquioxanes Reinforced Epoxy/Bismaleimide Hybrids Featuring High Thermal Stability, *Polymers*, 2022, **14**, 2380.
35 W. C. Chen, Y. T. Liu and S. W. Kuo, Highly Thermal Stable Phenolic Resin Based on Double-Decker-Shaped POSS Nanocomposites for Supercapacitors, *Polymers*, 2020, **12**, 2151.
36 W. C. Chen, M. M. M. Ahmed, C. F. Wang, C. F. Huang and S. W. Kuo, Highly thermally stable mesoporous Poly (cyanate ester) featuring double-decker-shaped polyhedral silsesquioxane framework, *Polymer*, 2019, **185**, 121940.
37 K. Wei, L. Wang and S. Zheng, Organic–inorganic polyurethanes with 3,13-dihydroxypropyloctaphenyl double-decker silsesquioxane chain extender, *Polym. Chem.*, 2013, **4**, 1491–1501.
38 B. Zhao, K. Wei, L. Wang and S. Zheng, Poly(hydroxyl urethane)s with Double Decker Silsesquioxanes in the Main Chains: Synthesis, Shape Recovery, and Reprocessing Properties, *Macromolecules*, 2020, **53**, 434–444.

39 N. Liu, L. Li, L. Wang and S. Zheng, Organic-inorganic polybenzoxazine copolymers with double decker silsesquioxanes in the main chains: Synthesis and thermally activated ring-opening polymerization behavior, *Polymer*, 2017, **109**, 254–265.

40 Y. T. Liao, Y. C. Lin and S. W. Kuo, Highly Thermally Stable, Transparent, and Flexible Polybenzoxazine Nanocomposites by Combination of Double-Decker-Shaped Polyhedral Silsesquioxanes and Polydimethylsiloxane, *Macromolecules*, 2017, **50**, 5739–5747.

41 W. C. Chen and S. W. Kuo, Ortho-Imide and Allyl Groups Effect on Highly Thermally Stable Polybenzoxazine/Double-Decker-Shaped Polyhedral Silsesquioxane Hybrids, *Macromolecules*, 2018, **51**, 9602–9612.

42 S. Wu, T. Hayakawa, R. Kikuchi, S. J. Grunzinger, M. Kakimoto and H. Oikawa, Synthesis and characterization of semiaromatic polyimides containing POSS in main chain derived from double-decker-shaped silsesquioxane, *Macromolecules*, 2007, **40**, 5698–5705.

43 C. W. Hsiao, A. M. Elewa, M. G. Mohamed and S. W. Kuo, Highly stable hybrid porous polymers containing polyhedral oligomeric silsesquioxane (POSS)/Dibenzo[g,p]chrysene and Dibenzo[b,d]thiophene units for efficient Rhodamine B dye removal, *Sep. Purif. Technol.*, 2024, **332**, 125771.

44 C. Y. Chen, M. G. Mohamed, W. C. Chen and S. W. Kuo, Construction of Ultrastable porous carbons materials derived from organic/inorganic double decker silsesquioxane (DDSQ) hybrid as a high-performance electrode for supercapacitor, *Mater. Today Chem.*, 2023, **34**, 101773.

45 C. Y. Chen, W. C. Chen, M. G. Mohamed, Z. Y. Chen and S. W. Kuo, Highly Thermally Stable, Reversible, and Flexible Main Chain Type Benzoxazine Hybrid Incorporating Both Polydimethylsiloxane and Double-Decker Shaped Polyhedral Silsesquioxane Units through Diels–Alder Reaction, *Macromol. Rapid Commun.*, 2023, **44**, 2200910.

46 S. Wu, T. Hayakawa, M. Kakimoto and H. Oikawa, Synthesis and Characterization of Organosoluble Aromatic Polyimides Containing POSS in Main Chain Derived from Double Decker Shaped Silsesquioxane, *Macromolecules*, 2008, **41**, 3481–3487.

